Evolution of Berry phase and half-metallicity in Cr_2Te_3 in response to strain, filling, thickness, and surface termination

Sohee Kwon,[1,*] Yuhang Liu,[1] Hang Chi,[2,3] Gen Yin,[4] Mahesh R. Neupane,[1,5,†] and Roger K. Lake[1,‡]

[1]*Laboratory for Terahertz & Terascale Electronics (LATTE), Department of Electrical and Computer Engineering, University of California-Riverside, Riverside, California 92521, USA*

[2]*Department of Physics, University of Ottawa, Ottawa, Ontario, Canada, K1N 6N5*

[3]*Nexus for Quantum Technologies, University of Ottawa, Ottawa, Ontario, Canada, K1N 6N5*

[4]*Department of Physics, Georgetown University, Washington, District of Columbia 20057, USA*

[5]*DEVCOM Army Research Laboratory, 2800 Powder Mill Road, Adelphi, Maryland 20783, USA*

(Received 13 January 2024; revised 27 March 2024; accepted 28 March 2024; published 19 April 2024)

Cr_2Te_3 is a ferromagnetic, quasi-two-dimensional layered material with perpendicular magnetic anisotropy, strong spin-orbit coupling, and nontrivial band topology. The nontrivial topology results in an intrinsic anomalous Hall conductivity (AHC) that switches sign under filling and biaxial strain. Thin films can exhibit half-metallicity. Using density-functional theory combined with maximally localized Wannier functions, we reveal the physical origins of the sensitivity of the sign of the AHC to strain and filling, and we determine the effect of surface termination on the half-metallicity. We find that thin films terminated on the Te layers are the most energetically stable, but only the thin films terminated on both sides with the partially occupied Cr layers are half metals. In bulk Cr_2Te_3, the sensitivity of the sign of the AHC to strain and filling results from the complex Fermi surface comprised of three bands. Filling of local minima and bands near anticrossings alters the local Berry curvature, consistent with the negative-to-positive switching of the AHC. Similarly, strain depopulates a local minimum, shifts a degenerate point closer to the Fermi energy, and causes two spin-orbit split bands to reverse their order. These findings provide a physical understanding of the evolution of the Berry phase, AHC, and half-metallicity in Cr_2Te_3.

DOI: 10.1103/PhysRevB.109.134430

I. INTRODUCTION

The magnetic structure of bulk Cr_2Te_3 has been extensively investigated for decades [1–7]. More recently, interest has shifted to thin films of Cr_2Te_3 [8–14]. Due to the van der Waals coupled $CrTe_2$ layers and unique self-intercalated Cr layers, $Cr_{1+x}Te_2$ is a promising candidate for modulating both its magnetic properties and topological properties [15].

Half-metallicity is an important feature in high-performance spintronic devices. In a half metal, there is a band gap in one spin channel and metallic behavior in the other. As a result, the electrons at the Fermi level are fully spin polarized. Within the Cr-Te family, half-metallic ferromagnetism was reported in bulk zinc blende CrTe [16]. There has been little focus on the effect of surface termination on the stability and half-metallicity in few-layer films. Bian *et al*. [11] found that $Cr_{1+\delta}Te_2$ thin films terminated by Te layers have in-plane lattice contraction compared to that of the bulk and to that of Cr-terminated films, and they concluded that few-layer films terminated with Te layers were unstable. They found that Cr-terminated Cr_2Te_3 films with thicknesses ranging from one monolayer to four layers exhibit half-metallic behavior.

The anomalous Hall conductivity (AHC) of various Cr-Te compounds has been actively studied. Huang *et al*. [17] reported an AHC of 67 kΩ cm and a corresponding anomalous Hall angle of 5.5% in a 170-nm-thick 1T-$CrTe_2$ flake at $T = 3$ K. It was determined that the large AHC originated from extrinsic skew scattering rather than from the intrinsic Berry phase. Fujisawa *et al*. [15] investigated $Cr_{1+\delta}Te_2$ thin films grown by molecular beam epitaxy (MBE) and tuned by the stoichiometry ratio in the range $0.3 < \delta < 0.8$. Angle-resolved photoemission spectroscopy measurements showed a relatively rigid shift of the Fermi energy (E_F) as a function of stoichiometry of $\Delta E_F/\Delta\delta \sim 1.54$ eV/atom. The sign of the AHC changed from positive to negative as δ varied from 0.33 to 0.47. The experimental values of the AHC qualitatively matched the calculated intrinsic AHC values, including the change of sign, although the calculated values were two orders of magnitude greater than the experimental ones.

Chi *et al*. [18] reported strain-tunable anomalous Hall conductivity in Cr_2Te_3 thin films. The growth of various thicknesses of Cr_2Te_3 films on Al_2O_3 and $SrTiO_3$ resulted in different levels of average strain. A sign reversal of the AHC was observed under compressive strain both experimentally and theoretically. The quantitative value of the AHC, calculated from the intrinsic Berry phase of the unstrained crystal, agreed with the experimental value. Furthermore, under the

*skwon054@ucr.edu

†mahesh.r.neupane.civ@army.mil

‡Corresponding author: rlake@ece.ucr.edu

application of compressive biaxial strain, the calculated intrinsic AHC was found to change sign, consistent with the experimental data.

Guillet *et al*. [19] demonstrated MBE growth of five monolayers of Cr_2Te_3 on sapphire and on various 2D substrates: graphene, WSe_2, and Bi_2Te_3. A sign change in the AHC was observed for samples on sapphire. Theoretically, a sign reversal of the AHC occurred as E_F was shifted by 10 meV with respect to its equilibrium value. Possible origins of the AHC sign reversal were suggested to be strain dependence, thermal broadening upon heating, and charge transfer due to the substrate effect. The authors claimed that the AHC was primarily from the intrinsic effect; however, the Berry phase analysis was not discussed in detail. The effect of strain was also studied theoretically by Gebredingle *et al*. [20] for Cr_2X_3 (X = S, Se, Te), although its affect on the AHC was not considered.

In this paper we determine the effect of surface termination on thin-film stability and half-metallicity. We then show how strain and band filling affect the electronic band structure and the Berry curvature, which is the physical origin of the sign reversal of the intrinsic AHC in bulk Cr_2Te_3.

II. METHODOLOGY

The first-principles electronic structure calculations are carried out within the projector augmented-wave method, as implemented in the Vienna *Ab Initio* Simulation Package (VASP) [21]. The generalized gradient approximation is used to describe the exchange-correlation functional as parametrized by Perdew, Burke, and Ernzerhof (PBE) [22]. The van der Waals interaction is included using the DFT-D3 method of Grimme *et al.* with zero damping [23]. We apply biaxial strain and relax the atomic positions within the unit cell. After relaxation, the forces acting on the ions are less than 5×10^{-3} eV/Å, and the change in the total energy between two ionic relaxation steps is smaller than 10^{-6} eV. The high-symmetry k path has been chosen by the AFLOW software [24]. With a cutoff energy of 520 eV, we use a converged Monkhorst Pack $8 \times 8 \times 4$ k grid for geometric relaxation and a Γ-centered $12 \times 12 \times 6$ k grid for the electronic calculation, including spin-orbit coupling (SOC).

Figures 1(a) and 1(b) display a top and cross-sectional view of the hexagonal unit cell of bulk Cr_2Te_3, consisting of 8 Cr atoms and 12 Te atoms. The Brillouin zone, and the high-symmetry paths, are shown in Fig. 1(c). The space group of bulk Cr_2Te_3 is $P\bar{3}1c$ (No. 163) with sixfold in-plane symmetry [18]. The unit cell consists of alternating layers in which all of the metal sites are either fully occupied with Cr atoms or partially occupied with Cr atoms. The partially occupied layers are also referred to as "vacancy layers" or "interstitial layers." There are three inequivalent Cr atoms in the unit cell. The Cr atoms in the two vacancy layers are equivalent and labeled as Cr_1. The fully occupied layers contain two inequivalent Cr atoms. The Cr atoms directly above and below the Cr_1 atoms are labeled as Cr_2. The Cr atoms at the corners and edges of the fully occupied layers are labeled as Cr_3. In the unstrained state, the optimized lattice constants of bulk Cr_2Te_3 are $a = 6.799$ Å and $c = 12.022$ Å . Structural stability is checked by performing phonon spectra and molecular

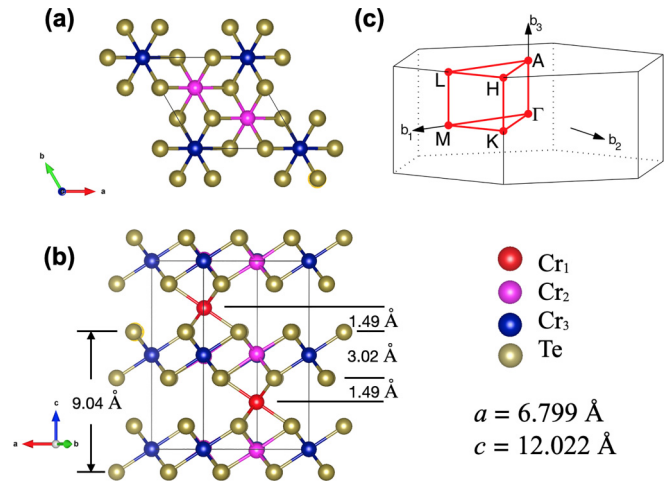

FIG. 1. (a) Top (001) and (b) side (210) views of bulk Cr_2Te_3. Interlayer distances are shown. The vertical and horizontal thin lines in (a), (b) show the unit cell from the (001) and (210) directions. The legend provides the labels for the three nonequivalent Cr atoms in the unit cell. The values for the a and c lattice constants and the interlayer distances of the fully relaxed structure are also shown. (c) The Brillouin zone and the high-symmetry lines used for plotting band structure and Berry phase.

dynamics calculations. The phonon dispersion is calculated using the second-order interatomic force constants (IFCs) and the finite displacement method as implemented in PHONOPY [25]. *Ab initio* molecular dynamics (AIMD) calculations, as implemented in VASP, are performed applying a canonical ensemble with a Nose-Hoover thermostat at room temperature. To choose the Hubbard U parameter for the Cr atoms, we investigate values of U ranging from 0 to 4 eV. As the value of U increases, the average magnetic moments per Cr ion increase monotonically from 2.85 μ_B to 3.10 μ_B while the magnetic anisotropy energy (MAE) decreases monotonically from 1.4×10^6 J/m^3 to -7×10^5 J/m^3. The values are plotted in Fig. 2. The MAE changes sign at $\sim U = 2$ eV, at which point out-of-plane anisotropy (easy axis along the

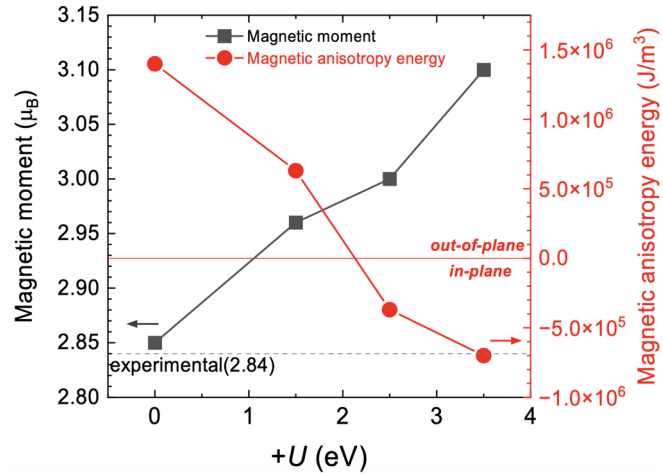

FIG. 2. Average magnetic moment per Cr atom (left axis) and magnetic anisotropy (right axis) as a function of $+U$ parameters of the Cr atom. Magnetic moments are in units of Bohr magnetons (μ_B).

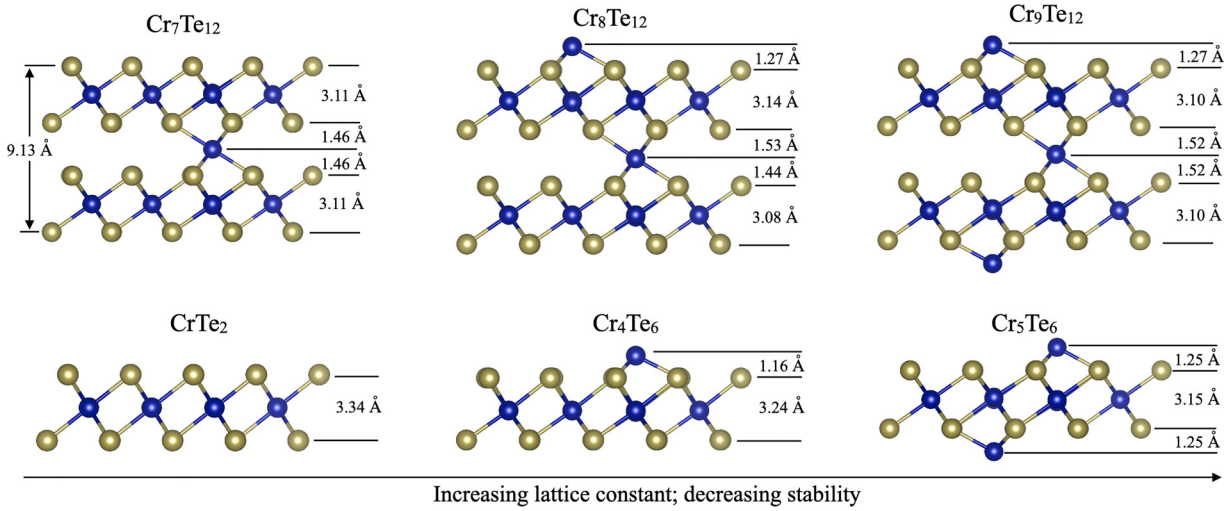

FIG. 3. Side views of the thin-film structures arranged from left to right in order of increasing in-plane lattice constant and decreasing stability. Interlayer distances are shown.

c axis) gives way to easy-plane anisotropy in the a-b plane. According to experimental results [18], bulk Cr_2Te_3 has a strong out-of-plane magnetic anisotropy and a magnetic moment per Cr atom of 2.82 μ_B [1]. With $U = 0$ eV, we obtain magnetic moments of 2.85 μ_B per Cr atom and an out-of-plane MAE of 0.5 meV per Cr atom. We also calculated the AHC using a value of $U = 2$ eV, and the result differs from the experimentally measured value by a factor of 10 as shown in Table IV of Appendix B. Therefore, $U = 0$ is used for all of the calculations in this paper.

The WANNIER90 package [26–29] is used to transform the Hamiltonian into the Wannier basis and to calculate topological properties, such as the Berry curvature and the AHC, with a denser k mesh of $100 \times 100 \times 100$. The AHC k-convergence test results are shown in Appendix B. We employ maximally localized Wannier functions (MLWFs), including Cr d-orbitals and Te p-orbitals. For MLWF calculations, we set the magnetization along the z axis and include SOC. With five d orbitals $\times 2$ spins per Cr atom and three p orbitals $\times 2$ spins per Te atom, the resulting Wannier basis consists of 152 orbitals per unit cell. The Hamiltonian matrix elements $\langle m, 0|H|n, \mathbf{R}\rangle$ and the Wigner-Seitz cell degeneracies $N_D(\mathbf{R})$ determined from WANNIER90 are used to construct the Hamiltonian in the Bloch-sum basis, $H^W_{mn}(\mathbf{k}) = \sum_{\mathbf{R}} \langle m, 0|H|n, \mathbf{R}\rangle e^{i\mathbf{k}\cdot\mathbf{R}}/N_D(\mathbf{R})$. The eigenvalues of $H^W_{mn}(\mathbf{k})$ are used to generate the multiple slices of the Fermi surface, with each slice calculated on a $400 \times 400\,k$ grid.

For current in the a-b plane, the intrinsic AHC is governed by the z component of Berry curvature $[\Omega^z(k)]$, which can be expressed as [30]

$$\Omega^z_n(\mathbf{k}) = \sum_{n' \neq n} \left[\frac{\langle \psi_{n\mathbf{k}}|v_x|\psi_{n'\mathbf{k}}\rangle\langle\psi_{n'\mathbf{k}}|v_y|\psi_{n\mathbf{k}}\rangle}{(\omega_{n'\mathbf{k}} - \omega_{n\mathbf{k}})^2} - \frac{\langle \psi_{n\mathbf{k}}|v_y|\psi_{n'\mathbf{k}}\rangle\langle\psi_{n'\mathbf{k}}|v_x|\psi_{n\mathbf{k}}\rangle}{(\omega_{n'\mathbf{k}} - \omega_{n\mathbf{k}})^2} \right], \quad (1)$$

$$= -2\mathrm{Im} \sum_{n' \neq n} \frac{\langle \psi_{n\mathbf{k}}|v_x|\psi_{n'\mathbf{k}}\rangle\langle\psi_{n'\mathbf{k}}|v_y|\psi_{n\mathbf{k}}\rangle}{(\omega_{n'\mathbf{k}} - \omega_{n\mathbf{k}})^2}, \quad (2)$$

where v is the velocity operator, n is the band index, and the band energy at wave vector $\mathbf{k}$ is $E_{n\mathbf{k}} = \hbar\omega_{n\mathbf{k}}$. The intrinsic AHC is determined from the sum of $\Omega^z_n(\mathbf{k})$ over the occupied bands,

$$\Omega^z(\mathbf{k}) = -\sum_n f_n(\mathbf{k})\Omega^z_n(\mathbf{k}), \quad (3)$$

where $f_n(\mathbf{k})$ is the occupation of band n at wave vector $\mathbf{k}$. The intrinsic AHC is obtained by integrating $\Omega^z(\mathbf{k})$ over the Brillouin zone:

$$\sigma_{xy} = -\frac{e^2}{\hbar}\int_{BZ} \frac{d^3k}{(2\pi)^3}\Omega^z(\mathbf{k}). \quad (4)$$

III. RESULTS AND DISCUSSION

A. Structural stability and half-metallicity in thin films $Cr_{1+\delta}Te_2$

The formation energies, lattice constants, and magnetic properties of finite slab structures are affected by the surface termination. We first consider the effect of surface termination on the structural stability of few-layer films. We calculate the formation energies and in-plane lattice constants for different surface terminations and layer numbers, and we also calculate the phonon dispersions and perform *ab initio* molecular dynamics to confirm structural stability at room temperature. The results from the phonon and molecular dynamics calculations are displayed in Appendix A.

We investigated three different types of terminations of the top/bottom $Cr_{1+\delta}Te_2$ slab surfaces: Te/Te, Cr/Te, and Cr/Cr. Figure 3 shows the structures considered for monolayer and bilayer $Cr_{1+\delta}Te_2$ with different surface terminations. The interlayer distances are also shown. The structures are arranged from left to right in the order of decreasing stability. Table I shows in-plane lattice constants, vertical heights, the in-plane, perpendicular, and hydrostatic strains (defined with respect to the bulk distances), formation energies, and formation energies per atom.

The formation energy is calculated from

$$E_{\mathrm{form}} = E_{\mathrm{total}} - (nE_{\mathrm{Cr}} + mE_{\mathrm{Te}}), \quad (5)$$

TABLE I. In-plane lattice constant a, vertical height h with the equivalent bulk distance in parentheses, formation energy E_{form}, and formation energy per atom for the slab structures in Fig. 3 and for bulk $Cr_{1+\delta}Te_2$. The quantities $\epsilon_\parallel$, $\epsilon_\perp$, and $\Delta\Omega/\Omega_{\text{bulk}}$ are the in-plane, out-of-plane, and volumetric percent changes with respect to the bulk values.

System	1L $CrTe_2$	1L Cr_4Te_6	1L Cr_5Te_6	2L Cr_7Te_{12}	2L Cr_8Te_{12}	2L Cr_9Te_{12}	Bulk Cr_2Te_3
Cr(Te) per u.c.	3(6)	4(6)	5(6)	7(12)	8(12)	9(12)	8(12)
In-plane a (Å)	6.350	6.638	6.849	6.668	6.726	6.812	6.799
$\epsilon_\parallel = \frac{a-a_{\text{bulk}}}{a_{\text{bulk}}}(\%)$	–6.6	–2.4	0.7	–1.9	–1.1	0.2	0
Vertical h (Å)	3.34(3.02)	4.40(4.52)	5.66(6.01)	9.13(9.04)	10.47(10.53)	11.74(12.02)	12.02
$\epsilon_\perp = \frac{h-h_{\text{bulk}}}{h_{\text{bulk}}}(\%)$	10.4	–2.7	–5.8	1.0	–0.6	–2.3	0
$\Delta\Omega/\Omega_{\text{bulk}}(\%)$	–3.8	–7.2	–4.4	–2.4	–2.7	–2.0	0
E_{form} (eV)	–3.270	–2.240	–1.098	–8.612	–7.427	–6.335	–10.818
E_{form}/atom (meV)	–363	–224	–100	–453	–371	–302	–541

where $n(m)$ is number of Cr(Te) atoms in a unit cell, and $E_{\text{Cr}}(E_{\text{Te}})$ is the single atom energy obtained from the total energy per atom of the bulk crystal of Cr(Te). The calculated values are $E_{\text{Cr}} = -9.528$ eV and $E_{\text{Te}} = -3.144$ eV. The formation energy per atom is $E_{\text{form}}/(n+m)$. The formation energies are defined such that more negative values correspond to greater stability. The results in Table I show that the structures terminated on the Te layers have the lowest formation energies in both monolayer and bilayer structures. Thus, the order of stability of both monolayer and bilayer films, arranged in decreasing order, is Te/Te-terminated > Te/Cr-terminated > Cr/Cr-terminated. While the Te/Te-terminated films are most stable, all terminations are stable at room temperature, as shown by the molecular dynamics calculations in Appendix A. Thus, it is likely that all terminations can be found in experiments.

The changes in the optimized in-plane lattice constants and vertical interlayer distances also have monotonic dependencies on the layer terminations, but in opposite directions. The in-plane lattice constants of the Te/Te-terminated films ($CrTe_2$ and Cr_7Te_{12}) decrease, and the vertical heights between the highest and lowest Te layers increase with respect to the bulk values. For the Cr/Cr-terminated films (Cr_5Te_6 and Cr_9Te_{12}), the opposite is true. The in-plane lattice constants slightly increase, and the vertical heights significantly decrease with respect to that of the bulk. In both of the above cases, the change in the in-plane and out-of-plain dimensions have opposite signs, as would be expected to preserve volume. For the Janus-type Te/Cr termination, the changes in both the in-plane and out-of-plane dimensions are negative. This could be seen as the behavior of an auxetic material with a negative Poisson's ratio [31–33]; however, as we discuss further below, this behavior is better viewed as a surface effect due to the Cr termination.

These trends are quantified in terms of the in-plane, out-of-plane, and volumetric percent changes with respect to the bulk values: $\epsilon_\parallel$, $\epsilon_\perp$, and $\Delta\Omega/\Omega_{\text{bulk}}$. The definitions are given in the left column of Table I. While we are using the symbols generally used for strain, we emphasize that these quantities are simply percent changes with respect to the equivalent bulk quantities. They are not actual strain, since each slab is fully relaxed. The in-plane percent change $\epsilon_\parallel$ is large and negative for the Te/Te-terminated films, and it becomes small and positive for the Cr/Cr-terminated films. The out-of-plane percent change $\epsilon_\perp$ is large and positive for the Te/Te-terminated films, and it becomes large and negative for the Cr/Cr-terminated films. For all structures, the volumetric percent change $\Delta\Omega/\Omega_{\text{bulk}} \approx 2\epsilon_\parallel + \epsilon_\perp$ is negative. For the monolayer (1L) structures, the magnitude of the volumetric percent change is smallest for Te/Te termination, because of the compensating signs and magnitudes of $\epsilon_\parallel$ and $\epsilon_\perp$. For the bilayer (2L) structures, the magnitude of the volumetric percent changes for Cr/Cr and Te/Te termination are comparable, –2.0 and –2.4, respectively. For both 1L and 2L structures, the magnitudes of volumetric percent changes are maximum for the Te/Cr-terminated structures, since the signs of $\epsilon_\parallel$ and $\epsilon_\perp$ are both negative.

There are two competing trends that determine the percent changes in the vertical heights of the slabs with respect to that of the bulk: the vertical expansion of the $CrTe_2$ layers and the large contraction of the vertical distances of the surface Cr layers. The thickness of the bulk $CrTe_2$ layer is 3.02 Å (see Fig. 1). For the monolayers (bottom row of Fig. 3), the vertical expansion is largest for the single $CrTe_2$ monolayer (3.34 Å), and it decreases as Cr atoms are added to the top and bottom surfaces. For the bilayers, all of the $CrTe_2$ layers are slightly expanded compared to that of the bulk, but the trend with respect to the addition of Cr surface layers is weak or nonexistent. The qualitative behavior of the expansion of the $CrTe_2$ layer is identical to that observed when comparing bulk 1T-$CrTe_2$ to bilayer and monolayer 1T-$CrTe_2$ [34].

The opposing trend is the reduction of the distance of the partially occupied Cr surface layer from the Te layer. In the bulk, the Cr_1-Te interlayer distance is 1.49 Å (see Fig. 1). In the Cr_8Te_{12} and Cr_9Te_{12} bilayers, that distance shrinks by –15% to 1.27 Å. In the monolayers, the shrinkage is slightly larger. It is the large vertical contraction of this surface Cr layer distance that causes $\epsilon_\perp$ to be negative for all of the structures terminated on at least one surface with Cr, i.e., the Cr/Te and Cr/Cr structures. This is the reason for the unusual trend present in the 1L and 2L Cr/Te-terminated structures in which both $\epsilon_\parallel$ and $\epsilon_\perp$ are negative.

Another distinguishing feature of $Cr_{1+\delta}Te_2$ thin films is half-metallicity. The density of states of differently terminated thin films are depicted in Fig. 4. The Te/Te-terminated monolayer $CrTe_2$ [Fig. 4(g)] and bilayer Cr_7Te_{12} [Fig. 4(a)]

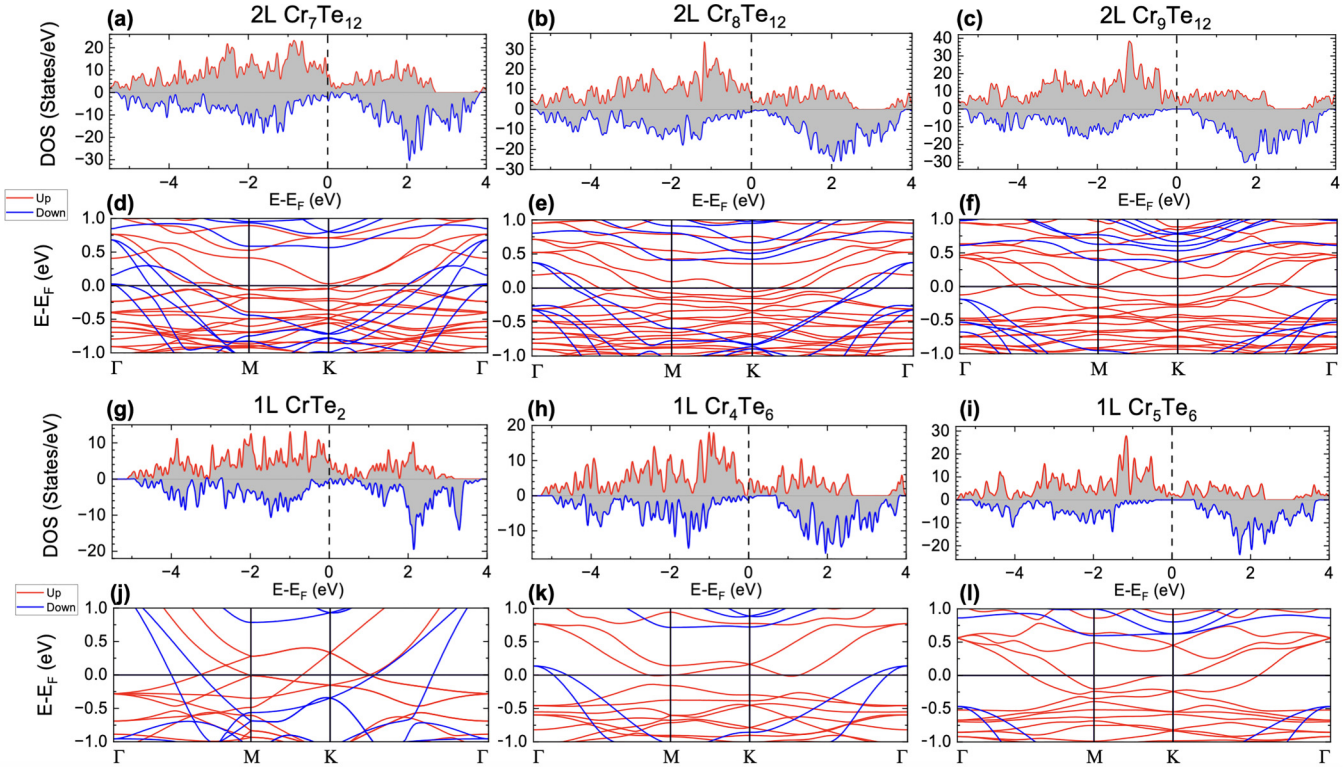

FIG. 4. Spin-resolved density of states and electronic band structures of differently terminated $Cr_{1+\delta}Te_2$ few-layer films. Red (blue) indicates the majority (minority) spin channel for both the density of states and the electronic band structure (E-k) plots. The density of states of Te/Te-, Cr/Te-, and Cr/Cr-terminated bilayers are shown in (a)–(c), respectively, and the corresponding E-k plots are shown in (d)–(f). The spin-resolved density of states of Te/Te-, Cr/Te-, and Cr/Cr-terminated monolayers are shown in (g)–(i), and the corresponding E-k plots are shown in (j)–(l).

have both majority- and minority-spin states at the Fermi level. In the Cr/Te-terminated monolayer and bilayer Cr_2Te_3 structures, the density of minority-spin states at the Fermi energy is low, as shown in Figs. 4(b) and 4(h). The electronic band structures of these monolayer and bilayer Cr/Te-terminated films in Figs. 4(e) and 4(k) show that two minority-spin hole bands cross the Fermi level near Γ. Adding another partially occupied Cr layer on the bottom surface, such that both surfaces are Cr terminated, the thin films become half metals, as shown in Figs. 4(c) and 4(i). The minority-spin hole bands at Γ are now 0.19 eV (0.47 eV) below the Fermi energy for the 2L (1L) structures, and the bands crossing the Fermi level are all majority carrier bands. The spin gap of monolayer Cr_5Te_6 is 1.07 eV and that of bilayer Cr_9Te_{12} is 0.55 eV, as shown in Figs. 4(f) and 4(l). The Cr added to the Te-terminated surfaces acts as a donor dopant, since it raises the Fermi level with respect to the existing bands, and it also increases the minority-spin gap between the minority-spin valence band at Γ and the minority-spin conduction band at M. These results are consistent with the electronic structure of bulk CrTe, which is a half-metallic ferromagnet [16], since adding extra Cr layers on the surfaces of the Cr_2Te_3 thin films makes their stoichiometry closer to that of CrTe.

B. Anomalous Hall conductivity and Berry curvature in bulk Cr_2Te_3

The sign of the AHC is sensitive to both band filling and strain. We will show that the origin of the sensitivity results from the filling, emptying, and shifting of three bands that cross the Fermi level. We now calculate the changes in the AHC of bulk Cr_2Te_3 resulting from filling and strain, and then analyze the changes by determining the effect of filling and strain on the electronic band structure and Berry curvature.

The calculated values of the AHC as a function of the Fermi level with respect to the equilibrium Fermi level for different values of biaxial strain are shown in Fig. 5. There exists a general trend that the AHC becomes more positive with filling for all strains. For the unstrained case, we will analyze the effect of filling by analyzing the band structure and Berry curvature at the two points indicated by the black square and red star in Fig. 5. For 0% strain, the value of the intrinsic AHC is $-12.7\ \Omega^{-1}\,\mathrm{cm}^{-1}$, which is in close agreement with the experimentally measured value of $-11.5\ \Omega^{-1}\,\mathrm{cm}^{-1}$ [18]. As the strain changes from $+1\%$ to -1%, the sign of the AHC switches from negative to positive. These results are in agreement with recently reported experiments [15,18,19].

A common metric used to quantify the magnitude of the AHC is the anomalous Hall angle (AHA). The strain

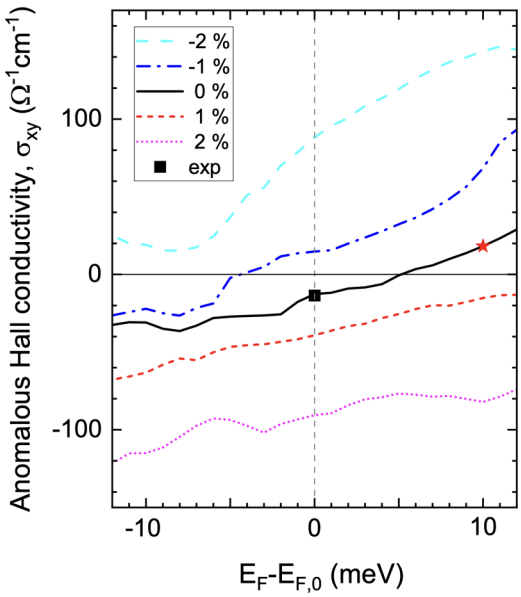

FIG. 5. Anomalous Hall conductivity as a function of the Fermi energy for different biaxial strains, as indicated in the legend. Negative (positive) values are for compressive (tensile) strain. The black square is the experimental value for the AHC in a bulklike Cr_2Te_3 sample (24 u.c.) from Ref. [18]. The point at $E_F - E_{F,0} = 10$ meV indicated by the red star is discussed in the text.

dependent anomalous Hall angles for different strains are shown in Table II. The AHA is determined by the relative contribution of the anomalous Hall current with respect to the normal current, expressed by $\Theta_{\mathrm{AH}} = \frac{\sigma_{xy}^{\mathrm{AH}}}{\sigma_{xx}}$. We obtained the experimental ρ_{xx} values from [18] for a 3-unit-cell (u.c.) thick film under compressive strain (0.493 mΩ cm) and a 24-u.c.-thick film that was unstrained (0.296 mΩ cm). To calculate the AHA, we use the average of these two values (0.394 mΩ cm) for all values of strain to eliminate the effect of different film thicknesses on ρ_{xx}. The calculated values of the AHA are comparable to those of bulk Cr_5Te_8 [35] but are relatively low among other magnetic materials such as Fe_3GeTe_2 [36].

Before analyzing how the Berry curvature changes with filling and strain, it is useful to first understand the relationship between the Berry curvature and the band structure of Cr_2Te_3 and determine which bands make significant contributions. From Eq. (1), it is clear that $\Omega_n^z(\mathbf{k})$ is antisymmetric in n and n'. Therefore only pairs of occupied and unoccupied bands contribute to the sum over n and n' leading to Ω^z. Furthermore, due to the denominator in (2), two bands closely spaced in energy on either side of the Fermi energy result in a strong peak in the Berry curvature and a large contribution to Ω^z. The sensitivity of the Berry curvature to small changes in the Fermi level further directs our attention to the bands near the Fermi level.

TABLE II. Calculated anomalous Hall angle. Experimental longitudinal resistivity ρ_{xx} is obtained from [18].

Strain	−1%	0%	1%
$\lvert\sigma_{xy}^{\mathrm{AH}}\rvert$ (Ω^{-1} cm^{-1})	14.7	12.7	39.2
Θ_{AH} (%)	0.58	0.50	1.55

The electronic band structure along the high-symmetry lines and the Berry curvature calculated along the same lines are shown in Fig. 6. One thousand k points are used for each line segment between high-symmetry points to resolve the sharp features in the Berry curvature. The shaded regions delineate the boundaries where the Berry curvature changes sign. These boundaries occur where a band crosses the Fermi level such that an unoccupied band becomes occupied, or vice versa. Since the integral over the entire Brillouin zone of the Berry curvature gives the AHC, which is rather small, the positive and negative regions of Berry curvature largely cancel. Thus, relatively small changes in any one region of the Brillouin zone can potentially cause a sign change in the AHC.

Two-dimensional slices of the Fermi surface at $k_z = 0$ (through Γ) and $k_z = b_3/2$ (the top of the Brillouin zone) are shown in Figs. 6(c) and 6(d). Cross sections of the Fermi surface over the top half of the Brillouin zone in steps of $\Delta k_z = b_3/20$ are shown in the Appendix C in Fig. 11. The plots are created by calculating the electronic band structure on a 400×400 $k_x - k_y$ grid and plotting $E_n(\mathbf{k})$ limited to the range $E_F \pm 2$ meV. Note that the linewidths of these curves are artifacts of the plotting software and have no physical meaning. The Fermi surface throughout the Brillouin zone consists of three bands. Of the 152 bands in the Wannier basis, only bands 115–117 cross the Fermi energy somewhere in the Brillouin zone. These three color-coded bands comprise the Fermi surface. Each color, red, blue, and green, identifies a single band and the corresponding band energies we designate as $E_r(\mathbf{k})$, $E_b(\mathbf{k})$, and $E_g(\mathbf{k})$, respectively. The bands are ordered such that at each $\mathbf{k}$, $E_r < E_b < E_g$. For example, in the $\mathbf{k}$ region of the blue band, the red band lies below E_F and the green band is above E_F. When a band has multiple nonconnected parts, it is a result of the band having multiple valleys. At the top of the Brillouin zone [Fig. 6(d)], there are two circular inner bands split by SOC. In the orbital projection plots [Figs. 6(e) and 6(f)], these are the bands crossing the Fermi level along the A-L and A-H lines. They are primarily Cr d-orbital bands, although they do have some Te p-orbital component. At $k_z = 0$, the orbital weight of these two bands becomes primarily p_x, p_y from the Te p-orbital bands. In the orbital projection plots, these are the first two bands crossing E_F along the Γ-M and Γ-K lines. The third band near the edge of the Brillouin zone in Fig. 6(d) retains a large d-orbital component at $k_z = 0$; however, the component changes from d_{yz} at the top of the Brillouin zone to primarily d_{z^2}, p_z at $k_z = 0$.

The two SOC split inner bands in Fig. 6(d) give rise to an intense ring of Berry curvature. The splitting of the two bands depends on the angle with respect to the k_x axis with a 60° rotational periodicity. The splitting is largest along the A-H line, since the Fermi level lies just below the anticrossing within the number-2 circle in Fig. 6(b). The splitting is smallest along the A-L line where the two bands are split in energy by 3 meV, where they cross the Fermi level within the number-3 circle in Fig. 6(b). These closely split bands give rise to the large

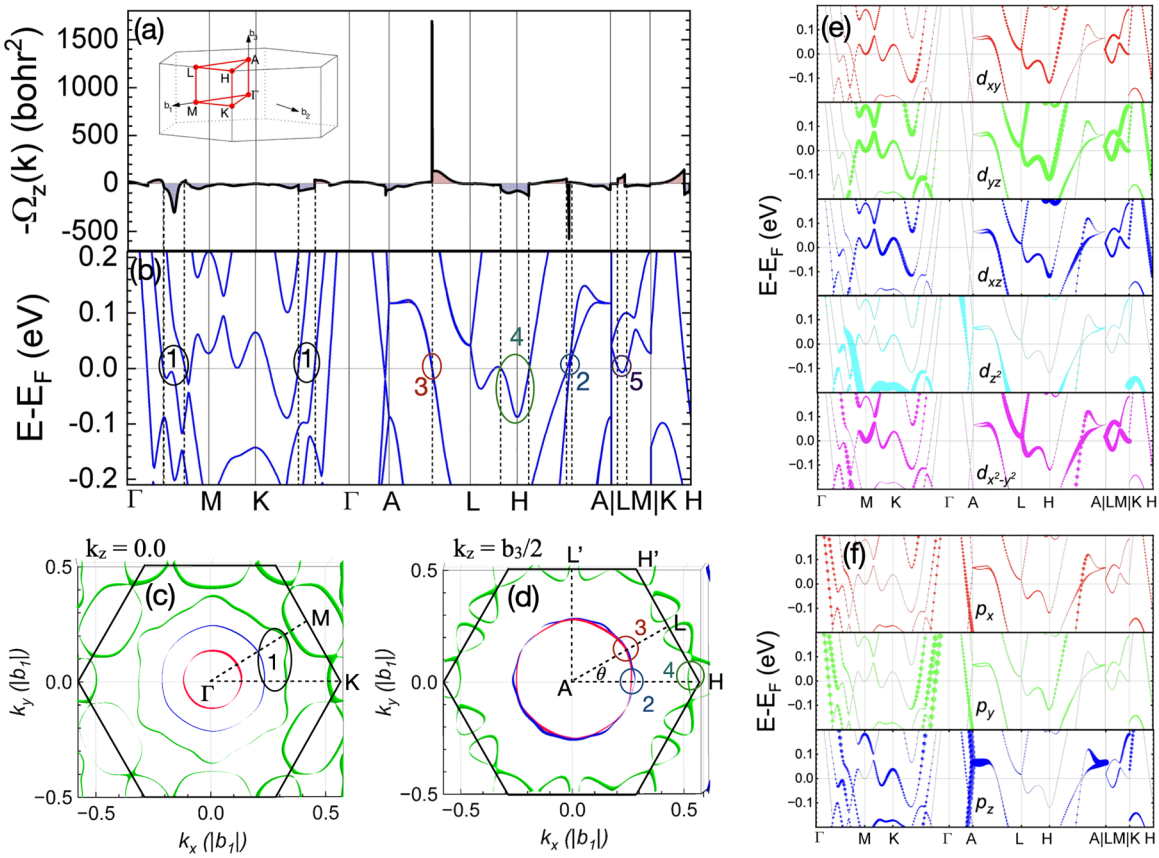

FIG. 6. (a) Berry curvature calculated along the high-symmetry lines corresponding to the (b) electronic dispersion. Cross sections of the Fermi surface are shown in (c) for $k_z = 0$ (through Γ) and (d) for $k_z = b_3/2$ (the top of the Brillouin zone). The three bands are color coded. The numbered circled regions correspond to the same numbered circled regions in (b). (e) Cr d-orbital projections of the bands. (f) Te p-orbital projections of the bands.

positive and negative narrow peaks in the Berry curvature along the A-L and A-H lines, respectively, shown in Fig. 6(a). In the two-dimensional Brillouin zone, these peaks form a ring of intense Berry curvature that alternates in sign every 30°. Another region of broad negative Berry curvature arises from the filled local minimum of the third band enclosed in the number-4 circle in Figs. 6(b) and 6(d). As k_z decreases from the top of the Brillouin zone to Γ, the two inner bands diverge at the Fermi level in k space, and the third band has multiple valleys with multiple crossings of the Fermi level. There is one region of negative Berry curvature that lies in the region of the filled second band and empty third band, shown in the number-1 circles in Figs. 6(b) and 6(c). One other region that contributes to both the filling and strain dependence is the small valley between L and M enclosed in circle 5 in Fig. 6(b). If it depopulates, as it does under tensile strain, its contribution disappears. With this understanding of the basic features of the band structure and Berry curvature, we now discuss the changes with respect to filling and strain.

C. Evolution of the Berry curvature with filling

First, we analyze the effect of band filling on the Berry curvature. We focus on the Berry curvature in the Γ-M-L-A plane with 0% strain at $E_F = 0$ and $E_F = 10$ meV, corresponding to the black square and red star in Fig. 5, respectively. The Berry curvature plots are shown in Figs. 7(a) and 7(b), respectively. Since the geometric structures and Brillouin zones are identical in both cases, we can take the difference of the Berry curvature plots for the two different Fermi energies and plot it, as shown in Fig. 7(c). To analyze the "hot" regions in the difference plot, we calculate the electronic band structure along the paths in the Brillouin zone indicated by the black solid lines in Figs. 7(a)–7(c). The band structure for the upper line is shown in Fig. 7(e), and the band structure along the lower line is shown in Fig. 7(f). The black line in the inset of both figures shows the k-space path within the 3D Brillouin zone. Slices of the Fermi surface at these same two k_z values are shown in Figs. 7(g) and 7(h).

We now analyze the regions of large difference in Fig. 7(c) using the band structures calculated along the lines shown. First, consider the lower line in Fig. 7(c). It intersects the red difference regions at the circles labeled 1 and 2. These same regions are shown in the band structure in Fig. 7(f) and the Fermi surface in Fig. 7(h). The increase in the Berry curvature arises from a filling of the local electronlike minimum at the Fermi level. The filling of the states on either side of the minimum, lying between the red-dashed and solid black lines,

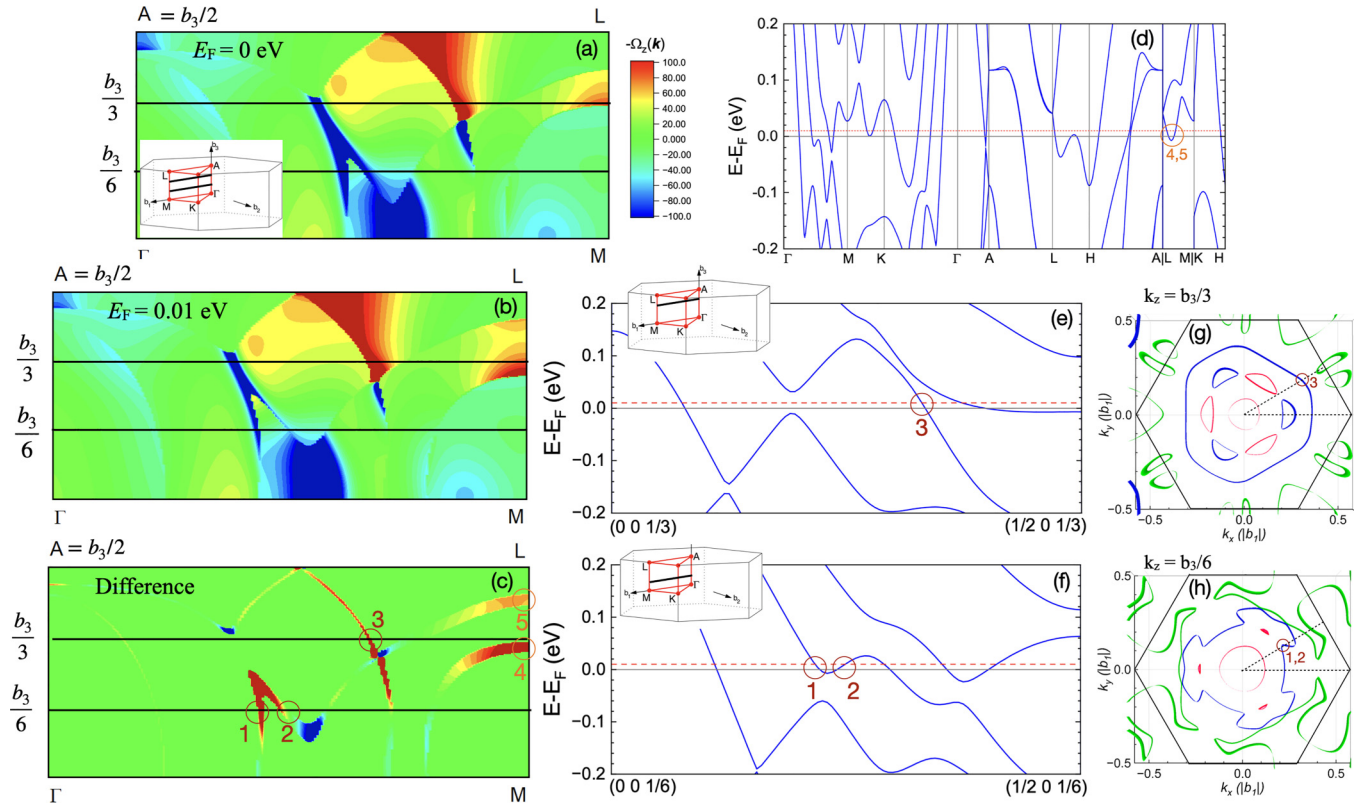

FIG. 7. (a), (b) Berry curvature contour plots in the two-dimensional Γ-A-L-M k plane for the equilibrium state ($E_F = 0$) (a) and $E_F =$ 10 meV (b). (c) Difference of the Berry curvature plots (a) and (b), $\Omega_z(k)[E_F(10\text{ meV})\text{-}E_F(0\text{ meV})]$. (c) Electronic band structure along the high-symmetry k paths for 0% strain. The red dashed line shows the Fermi level shifted upwards by 10 meV. The orange circle labeled 4,5 corresponds to the circles labeled 4 and 5 in (c). (e) Band structure calculated along the upper solid lines in (a)–(c) at $k_z = b_3/3$. The path in k space is shown in the inset. (f) Band structure calculated along the lower lines in (a)–(c) at $k_z = b_3/6$. The path in k space is shown in the inset. The x-axis labels in (e) and (f) are in units of the reciprocal lattice vectors. (g), (h) Two-dimensional slices of the Fermi surface at a fixed k_z as indicated by the labels on each plot. The labeled red circles in (g) and (h) correspond to the circles with the same labels in (e) and (f).

allows them to contribute to the sum in Eq. (2) as a filled state with a matrix element to an empty state that is closely spaced in energy. Next, consider the upper line in 7(c). It intersects the red difference region at the circle labeled 3. This same region is shown in the band structure in Fig. 7(e) and the Fermi surface in Fig. 7(g). The increase in the Berry curvature arises from the filling of the lower band near an anticrossing, so that there is an unoccupied band very close in energy. The final two circled regions 4 and 5 lie along the M-L path shown in Fig. 7(d). These two regions also arise from the filling of a local minimum that is close in energy to an unoccupied band, so that the additional filled states on either side of the minimum give rise to a large contribution to the Berry curvature. We will see that this is the same band that becomes unoccupied under tensile strain shown in Fig. 8(f).

D. Evolution of the Berry curvature with strain

Now, we consider the effect of strain on the Berry curvature and the electronic band structure. Figure 8 shows the Berry curvature and electronic band structures of bulk Cr_2Te_3 along the high-symmetry k paths for compressive (−1%) and tensile (+1%) strains. The vertical axes of the main plots in (a), (e) have been truncated so that other features can be observed, but the full plots are shown in the upper insets. As shown in Figs. 8(a) and 8(e), the sharp, narrow peak in the Berry curvature midway along the A-L line switches sign under tensile strain. The sign of the peak along the A-H line remains unchanged. Thus, the ring of intense Berry curvature along the top of the Brillouin zone no longer alternates in sign under tensile strain, but it is entirely negative. This sign change is consistent with the sign change of the AHC with strain. The bottom insets of Figs. 8(b) and 8(f) show a zoomed-in region near the Fermi level that illustrates the underlying mechanism for the change of sign. The change in strain causes the order of the two bands to switch, as denoted by the red and blue colors. We determine this by considering the inner product of the eigenvectors of $H^W(\mathbf{k})$ corresponding to the two bands near the Fermi energy under compressive and tensile strain. There are four eigenvectors ($|1,n\rangle$, $|2,n\rangle$, $|1,p\rangle$, $|2,p\rangle$) where the numbers 1 and 2 indicate the lower and upper band, respectively, and the letters n and p indicate compressive and tensile strain, respectively. We find that $|\langle 1n|2p\rangle|^2 = 0.57$ and $|\langle 1n|1p\rangle|^2 = 0.38$. Thus the lower energy band under compressive strain has a greater overlap with the upper energy band under tensile strain. This indicates a switching of the

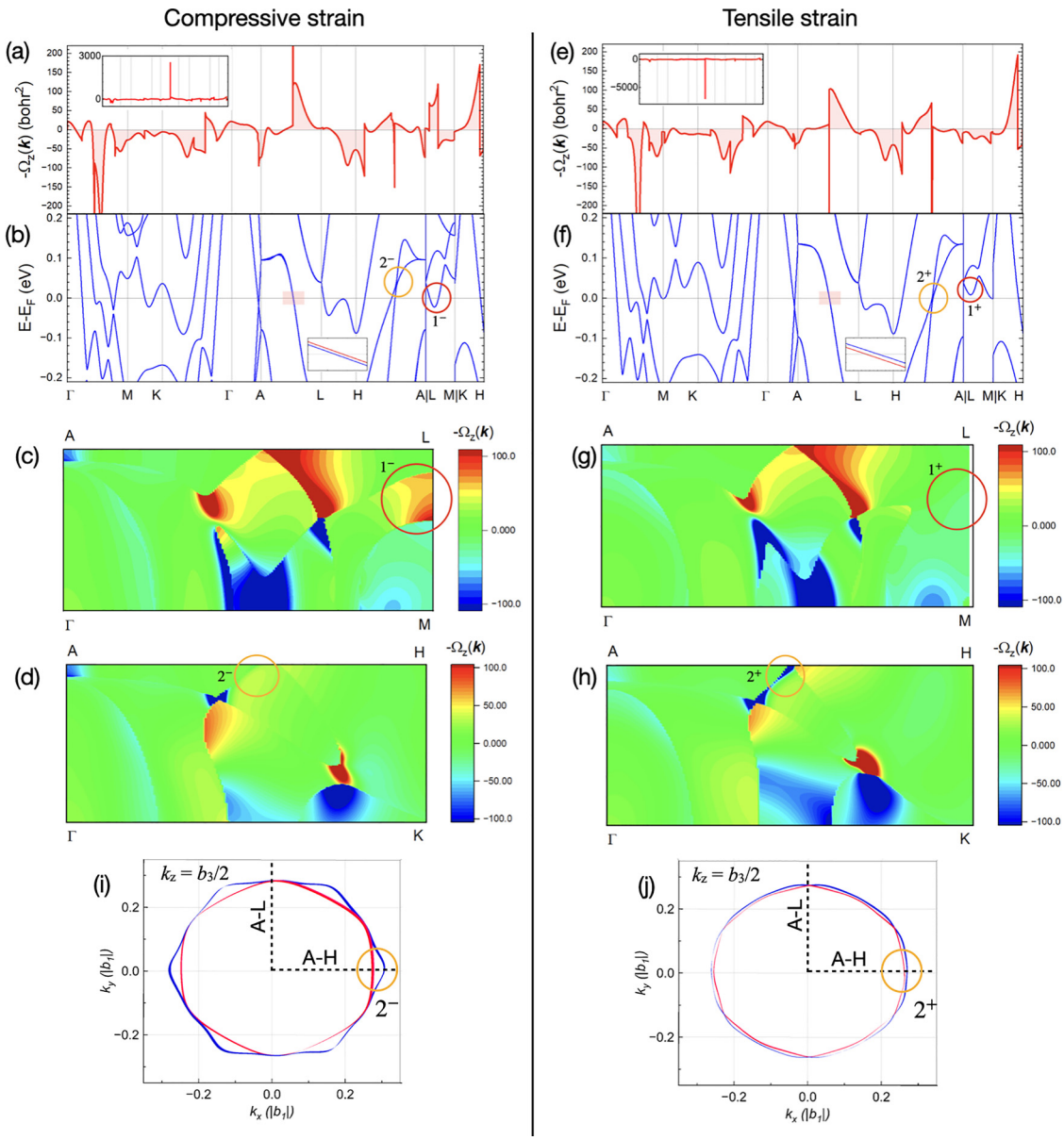

FIG. 8. All of the results in the left panel are calculated under 1% compressive strain, and all of the results in the right panel are calculated under 1% tensile strain. (a), (e) Berry curvature along high-symmetry lines of the Brillouin zone. The vertical axes are truncated for clarity. The top insets in (a), (e) show the same plots over the full range of the Berry curvature. (b), (f) Electronic band structure plotted along the same high-symmetry lines as the Berry curvature. The bottom insets in (b) and (f) show the zoomed-in area of highlighted rectangular regions in the middle of the A-L k path. Berry curvature plotted in the two-dimensional planes defined by the high-symmetry lines (c), (g) Γ-A-L-M and (d), (h) Γ-K-H-A. The two planes are illustrated in the inset of Fig. 7(f). The color bars show the signs and magnitudes of the Berry curvatures. (i), (j) Zoom-in of the two inner rings in the cross sections of the Fermi surfaces under compressive and tensile strain taken at the top of the Brillouin zone ($k_z = b_3/2$).

bands under strain. Since the numerator in the Berry curvature expression in Eq. (1) is antisymmetric in the band index, a reversal of the bands results in a change of sign of the resulting Berry curvature. This effect can also be seen in the cross sections of the Fermi surfaces under compressive and tensile strain shown in Figs. 8(i) and 8(j), respectively. Under compressive strain, the two bands in (i) never cross, whereas under tensile strain, the bands in (j) cross at each A-L line.

The peak in the Berry curvature along the A-H line is caused by the band crossing in the circles labeled $2^{\mp}$ in Figs. 8(b), 8(f) and 8(i), 8(j). As the strain changes from compressive to tensile, this band crossing moves closer to the Fermi level, which increases the magnitude of the local Berry curvature. The intrinsic AHC results from the integration of the Berry curvature over the entire Brillouin zone, and while these peaks have large magnitude, they are also very narrow. Therefore, we now consider the Berry curvature

in two different two-dimensional slices of the Brillouin zone.

The Berry curvature in the k-space planes bounded by the high-symmetry lines Γ-M-L-A and Γ-K-H-A are shown in Figs. 8(c), 8(d) 8(g), and 8(h). Strain changes the size of the unit cell and thus the Brillouin zones. Therefore, we are unable to take the difference of the two plots, as we did for filling, and instead make several observations based on visual comparison. Comparing the plots for compressive strain on the left to the ones for tensile strain on the right, there are two notable changes in the Berry curvature. There is a large positive Berry curvature along the M-L line under compressive strain that disappears under tensile strain, as shown in the red circled areas in Figs. 8(c) and 8(g). This is a result of the occupied band along M-L under compressive strain, shown in the 1^- circle in Fig. 8(b), becoming unoccupied under tensile strain, shown in the 1^+ circle in Fig. 8(f). Another contribution to the change in sign of the AHC comes from the band crossing, discussed above, circled in the $2^\mp$ circles in Figs. 8(b) and 8(f). Under compressive strain, the band crossing occurs above the Fermi level, and under tensile strain, the crossing occurs closer to the Fermi level. This results in a large negative contribution to the Berry curvature near the A-H line, shown in the region enclosed by 2^+ circle in Figs. 8(d) and 8(h). Thus, the change of sign of the AHC with strain is consistent with the shifts of the bands near the Fermi level, which either reduce the positive Berry curvature or create the regions of negative Berry curvature.

IV. CONCLUSION

In bulk Cr_2Te_3, we conclude that the sensitivity of the sign of the Berry curvature to strain and filling arises from the three bands that cross the Fermi level. There are multiple regions of positive and negative Berry curvature throughout the Brillouin zone that mostly cancel, so that small changes in the local Berry curvature can cause an overall sign change in the total integrated value, which determines the AHC. The intense ring of Berry curvature at the top of the Brillouin zone associated with the two SOC split bands is most striking. In the absence of tensile strain, the sign of the Berry curvature associated with the ring oscillates with each 30° rotation around the ring. Tensile strain causes a reversal of the band order along the A-L line such that the Berry curvature of the ring becomes uniformly negative. Other regions also contribute, and one that we have particularly identified comes from the local minimum along the M-L line at the face of the Brillouin zone. Tensile strain causes it to depopulate, which removes its positive contribution to the Berry curvature. The analysis of band filling shows that the changes in the Berry curvature, which drive the sign change in the AHC, occur throughout the Brillouin zone and that the largest changes in Berry curvature do not come from the ring. Filling (or depopulating) of local minima close to the unoccupied bands, or filling of bands near anticrossings, gives rise to the changes in the local Berry curvature that drive the sign change of the AHC with filling. In all cases, the contributions come from the change in filling of bands in close energetic proximity to unoccupied bands.

In thin films, termination with the Te layer gives the most stable structures, although thin films terminated with Cr are also stable. Terminating the surface at the partially occupied Cr layer increases the in-plane lattice constant, and it increases the spin polarization of the electrons at the Fermi level. Only when both surfaces are terminated at the partially occupied Cr layer do the thin films become half metals in one- and two-layer films. The Cr termination serves as a donor dopant moving the Fermi level into the minority-spin gap, and it also increases the magnitude of the minority-spin gap.

ACKNOWLEDGMENTS

This work was supported in part by the U.S. Army Research Laboratory (ARL) Research Associateship Program (RAP), Cooperative Agreement (CA) W911NF-16-2-0008. This work used STAMPEDE2 at TACC through allocation DMR130081 from the Advanced Cyberinfrastructure Coordination Ecosystem: Services & Support (ACCESS) program [37], which is supported by National Science Foundation Grants No. 2138259, No. 2138286, No. 2138307, No. 2137603, and No. 2138296.

APPENDIX A: PHONON DISPERSION AND MOLECULAR DYNAMICS CALCULATIONS

In order to confirm the structural stability of bulk and thin films of Cr_2Te_3, we calculate the phonon dispersion. A $2 \times 2 \times 2$ supercell with a k grid of $4 \times 4 \times 2$ is used for the bulk and a $2 \times 2 \times 1$ supercell with a k grid of $6 \times 6 \times 1$ is chosen for thin films. All thin-film unit cells contain a 15-Å-thick vacuum region. Figure 9(c) shows the phonon dispersion for bulk Cr_2Te_3, Figs. 9(a) and 9(b) show the phonon dispersions for bilayer thin films, and Figs. 9(d)–9(f) show the phonon dispersions for monolayer thin films. The phonon dispersion of (d) $CrTe_2$ was calculated by us previously, and it requires a Hubbard parameter of $U = 2$ eV to obtain a dispersion with non-negative frequencies (see the Supplemental Material of [34]). All of the other plots are calculated with $U = 0$. The phonon dispersions of all of these other few-layer structures show small regions of negative frequency near Γ, which is not unusual for these types of calculations.

Therefore, to further verify the stability of the thin films, especially with Cr termination, we perform AIMD calculations, as implemented in VASP. Using $2 \times 2 \times 1$ supercell and a temperature of 300 K, we perform AIMD calculations with a 1-fs time step over a period of 1 ps. Figure 10 shows temperature oscillations as a function of time at a constant average temperature of 300 K for Cr/Te- and Cr/Cr- terminated monolayer thin films. The insets of Fig. 10 show crystal structures at the beginning and the end of calculations. The final structures are slightly distorted; however, they maintain the same crystal structure, and all of the bonds are intact. These results indicate that both Cr_4Te_6 and Cr_5Te_6 thin films are thermodynamically stable.

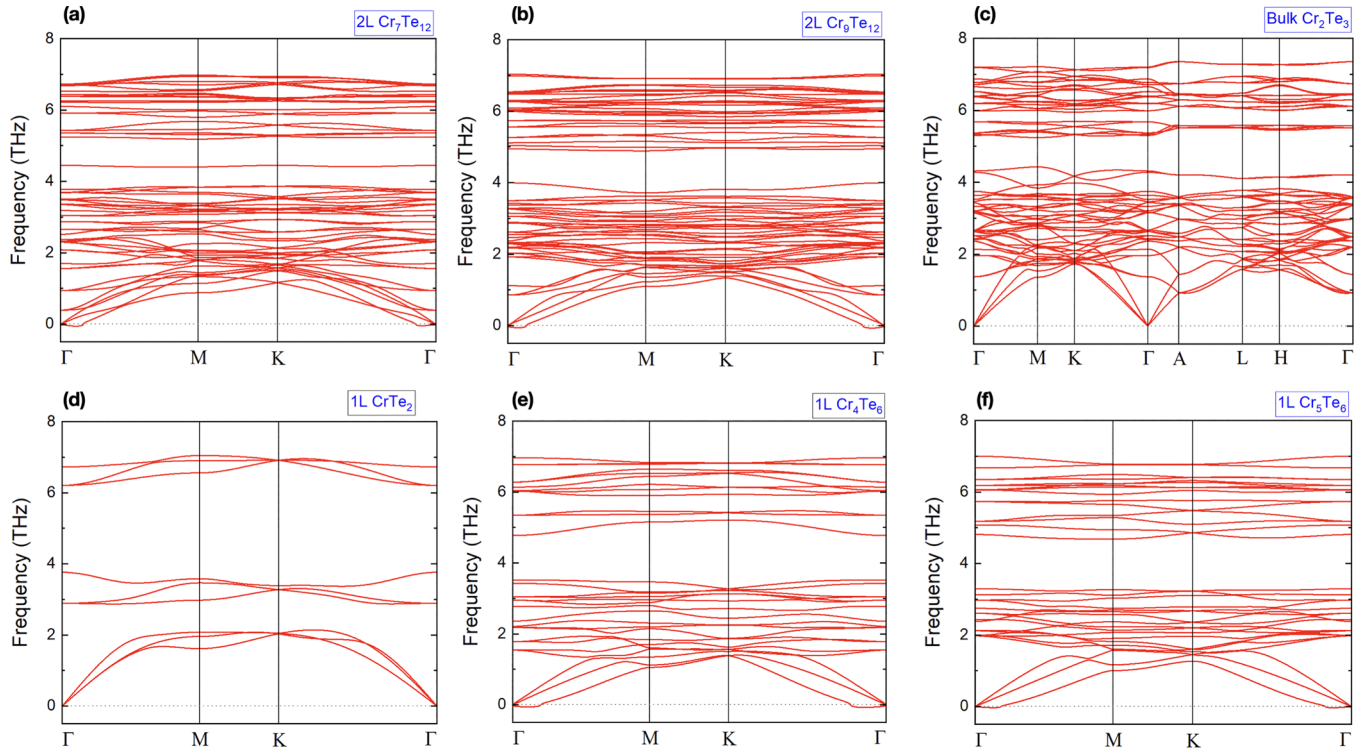

FIG. 9. Phonon dispersions of (a) 2L Cr_7Te_{12}, (b) 2L Cr_9Te_{12}, (c) bulk Cr_2Te_3, (d) 1L $CrTe_2$, (e) 1L Cr_4Te_6, and (f) 1L Cr_5Te_6.

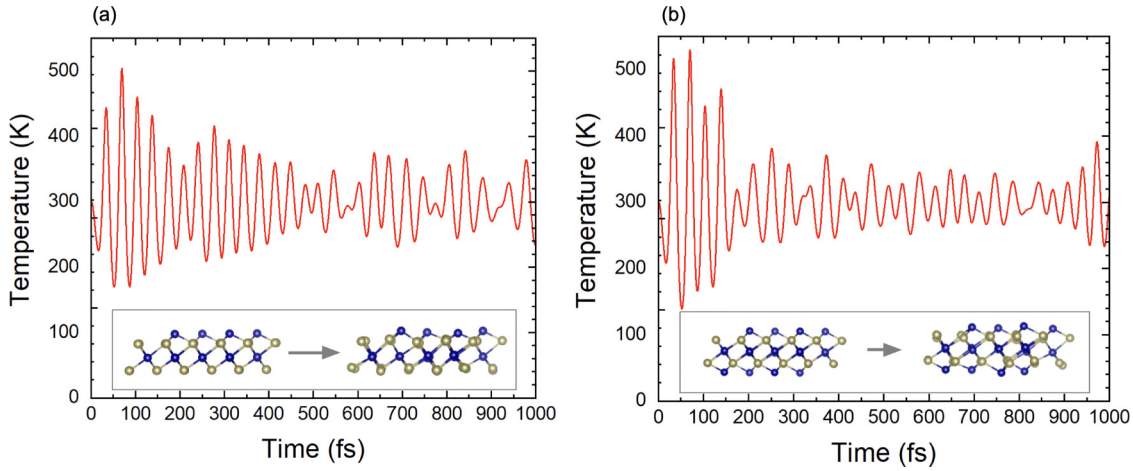

FIG. 10. Constant-temperature AIMD calculations for Cr/Te-terminated Cr_4Te_6 (a) and Cr/Cr-terminated Cr_5Te_6 (b). Red curve represents the temperature as a function of time. Insets show the crystal structures at 0 fs and 1 ps for each calculation.

TABLE III. Convergence of the AHC as a function of the k grid.

k mesh	Adaptive refinement	AHC (Ω^{-1} cm^{-1})
$40 \times 40 \times 40$	–	–9.53
$40 \times 40 \times 40$	$3 \times 3 \times 3$	–19.24
$50 \times 50 \times 50$	$3 \times 3 \times 3$	–12.65
$80 \times 80 \times 80$	–	–12.67
$100 \times 100 \times 100$	–	–12.7

TABLE IV. Experimental values [18] and calculated average magnetic moments and anomalous Hall conductivity for $U = 0$ and $U = 2$ eV.

	Experimental	$U = 0$ eV	$U = 2$ eV
Magnetic moment (μ_B)	2.84	2.85	3.1
AHC (Ω^{-1} cm^{-1})	–11.5	–12.7	–120.95

APPENDIX B: METHOD DETAILS

Table III shows the results of the k-grid convergence test for the calculation of the AHC. Table IV compares the experimentally known values of the magnetic moment and AHC with values calculated with $U = 0$ and $U = 2$ eV.

APPENDIX C: SLICES OF THE FERMI SURFACE AT FIXED k_z

Figure 11 shows slices of the Fermi surface of the top half of the Brillouin zone at fixed k_z in steps of $\Delta k_z = 0.1(b_3/2)$. The Brillouin zone projected onto the $k_x - k_y$ plane is outlined.

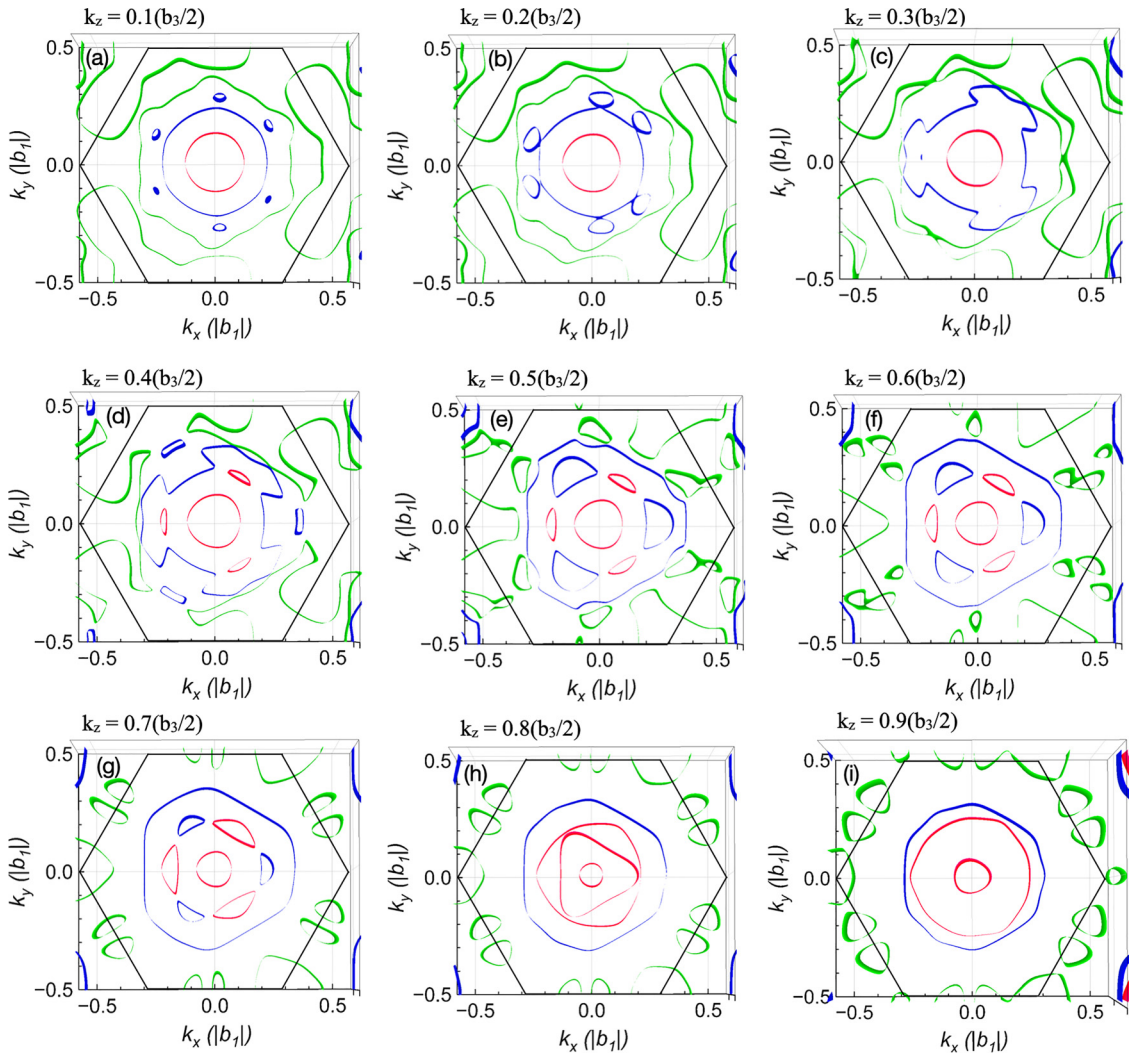

FIG. 11. Two-dimensional slices of the Fermi surface at different values of k_z as shown.

[1] A. F. Andresen, Acta Chem. Scand. **24**, 3495 (1970).

[2] T. Hashimoto, K. Hoya, M. Yamaguchi, and I. Ichitsubo, J. Phys. Soc. Jpn. **31**, 679 (1971).

[3] T. Hamasaki, T. Hashimoto, Y. Yamaguchi, and H. Watanabe, Solid State Commun. **16**, 895 (1975).

[4] J. Dijkstra, H. Weitering, C. Van Bruggen, C. Haas, and R. De Groot, J. Phys.: Condens. Matter **1**, 9141 (1989).

[5] H. Konno, Y. Adachi, and M. Yuzuri, Jpn. J. Appl. Phys. **32**, 308 (1993).

[6] S. J. Youn, S. K. Kwon, and B. I. Min, J. Appl. Phys. **101**, 09G522 (2007).

[7] L. Hui, S. T. Lim, J. F. Bi, and K. L. Teo, J. Appl. Phys. **111**, 07D719 (2012).

[8] R. Akiyama, H. Oikawa, K. Yamawaki, and S. Kuroda, Phys. Status Solidi C **11**, 1320 (2014).

[9] D. M. Burn, L. B. Duffy, R. Fujita, S. L. Zhang, A. I. Figueroa, J. Herrero-Martin, G. van der Laan, and T. Hesjedal, Sci. Rep. **9**, 10793 (2019).

[10] H. Li, L. Wang, J. Chen, T. Yu, L. Zhou, Y. Qiu, H. He, F. Ye, I. K. Sou, and G. Wang, ACS Appl. Nano Mater. **2**, 6809 (2019).

[11] M. Bian, A. N. Kamenskii, M. Han, W. Li, S. Wei, X. Tian, D. B. Eason, F. Sun, K. He, H. Hui, F. Yao, R. Sabirianov, J. P. Bird, C. Yang, J. Miao, J. Lin, S. A. Crooker, Y. Hou, and H. Zeng, Mater. Res. Lett. **9**, 205 (2021).

[12] J. Chen, L. Wang, M. Zhang, L. Zhou, R. Zhang, L. Jin, X. Wang, H. Qin, Y. Qiu, J. Mei, F. Ye, B. Xi, H. He, B. Li, and G. Wang, Nano Lett. **19**, 6144 (2019).

[13] J. Zhong, M. Wang, T. Liu, Y. Zhao, X. Xu, S. Zhou, J. Han, L. Gan, and T. Zhai, Nano Res. **15**, 1254 (2022).

[14] Y. Zhong, C. Peng, H. Huang, D. Guan, J. Hwang, K. H. Hsu, Y. Hu, C. Jia, B. Moritz, D. Lu, J.-S. Lee, J.-F. Jia, T. P. Devereaux, S.-K. Mo, and Z.-X. Shen, Nat. Commun. **14**, 5340 (2023).

[15] Y. Fujisawa, M. P. Almanza, C. H. Hsu, A. Mohamed, K. Yamagami, A. Krishnadas, F. C. Chuang, K. H. Khoo, J. Zang, A. Soumyanarayanan, and Y. Okada, Adv. Mater. **35**, 2207121 (2023).

[16] W.-H. Xie, Y.-Q. Xu, B.-G. Liu, and D. G. Pettifor, Phys. Rev. Lett. **91**, 037204 (2003).

[17] M. Huang, S. Wang, Z. Wang, P. Liu, J. Xiang, C. Feng, X. Wang, Z. Zhang, Z. Wen, H. Xu, G. Yu, Y. Lu, W. Zhao, S. A. Yang, D. Hou, and B. Xiang, ACS Nano **15**, 9759 (2021).

[18] H. Chi, Y. Ou, T. B. Eldred, W. Gao, S. Kwon, J. Murray, M. Dreyer, R. E. Butera, A. C. Foucher, H. Ambaye, J. Keum, A. T. Greenberg, Y. Liu, M. R. Neupane, G. J. de Coster, O. A. Vail, P. J. Taylor, P. A. Folkes, C. Rong, G. Yin *et al.*, Nat. Commun. **14**, 3222 (2023).

[19] Q. Guillet, L. Vojacek, D. Dosenovic, F. Ibrahim, H. Boukari, J. Li, F. Choueikani, P. Ohresser, A. Ouerghi, F. Mesple, V. Renard, J.-F. Jacquot, D. Jalabert, H. Okuno, M. Chshiev, C. Vergnaud, F. Bonell, A. Marty, and M. Jamet, Phys. Rev. Mater. **7**, 054005 (2023).

[20] Y. Gebredingle, M. Joe, and C. Lee, ACS Appl. Nano Mater. **5**, 10383 (2022).

[21] P. E. Blöchl, Phys. Rev. B **50**, 17953 (1994).

[22] J. P. Perdew, K. Burke, and M. Ernzerhof, Phys. Rev. Lett. **77**, 3865 (1996).

[23] S. Grimme, J. Antony, S. Ehrlich, and H. Krieg, J. Chem. Phys. **132**, 154104 (2010).

[24] W. Setyawan and S. Curtarolo, Comput. Mater. Sci. **49**, 299 (2010).

[25] A. Togo, F. Oba, and I. Tanaka, Phys. Rev. B **78**, 134106 (2008).

[26] N. Marzari and D. Vanderbilt, Phys. Rev. B **56**, 12847 (1997).

[27] I. Souza, N. Marzari, and D. Vanderbilt, Phys. Rev. B **65**, 035109 (2001).

[28] A. A. Mostofi, J. R. Yates, G. Pizzi, Y.-S. Lee, I. Souza, D. Vanderbilt, and N. Marzari, Comput. Phys. Commun. **185**, 2309 (2014).

[29] G. Pizzi, V. Vitale, R. Arita, S. Blügel, F. Freimuth, G. Géranton, M. Gibertini, D. Gresch, C. Johnson, T. Koretsune, J. Ibañez-Azpiroz, H. Lee, J.-M. Lihm, D. Marchand, A. Marrazzo, Y. Mokrousov, J. I. Mustafa, Y. Nohara, Y. Nomura, L. Paulatto *et al.*, J. Phys.: Condens. Matter **32**, 165902 (2020).

[30] Y. Yao, L. Kleinman, A. H. MacDonald, J. Sinova, T. Jungwirth, D.-s. Wang, E. Wang, and Q. Niu, Phys. Rev. Lett. **92**, 037204 (2004).

[31] L. Yu, Q. Yan, and A. Ruzsinszky, Nat. Commun. **8**, 15224 (2017).

[32] T. Jing, D. Liang, M. Deng, and S. Cai, J. Mater. Chem. C **8**, 10382 (2020).

[33] N. T. Hiep, C. Q. Nguyen, and N. N. Hieu, Appl. Phys. Lett. **123**, 092102 (2023).

[34] Y. Liu, S. Kwon, G. J. d. Coster, R. K. Lake, and M. R. Neupane, Phys. Rev. Mater. **6**, 084004 (2022). Data files containing the relaxed coordinates of the structures can be found at https://doi.org/10.5061/dryad.280gb5mxc.

[35] B. Tang, X. Wang, M. Han, X. Xu, Z. Zhang, C. Zhu, X. Cao, Y. Yang, Q. Fu, J. Yang, X. Li, W. Gao, J. Zhou, J. Lin, and Z. Liu, Nat. Electron. **5**, 224 (2022).

[36] K. Kim, J. Seo, E. Lee, K.-T. Ko, B. S. Kim, B. G. Jang, J. M. Ok, J. Lee, Y. J. Jo, W. Kang, J. H. Shim, C. Kim, H. W. Yeom, B. I. Min, B.-J. Yang, and J. S. Kim, Nat. Mater. **17**, 794 (2018).

[37] T. J. Boerner, S. Deems, T. R. Furlani, S. L. Knuth, and J. Towns, in *Practice and Experience in Advanced Research Computing (PEARC '23), July 23-27, 2023, Portland, OR, USA* (ACM, New York, NY, 2023), p. 173.